



Soil crusting: new insight from synchrotron 2D micro X-ray diffraction mapping of clay-particle orientation and mineralogy

Vincent Geoffroy, Baptiste Dazas, Eric Ferrage, Felisa Berenguer, Céline Boissard, Laurent Michot, Folkert van Oort, Emmanuel Tertre, Fabien Hubert

► To cite this version:

Vincent Geoffroy, Baptiste Dazas, Eric Ferrage, Felisa Berenguer, Céline Boissard, et al.. Soil crusting: new insight from synchrotron 2D micro X-ray diffraction mapping of clay-particle orientation and mineralogy. *Geoderma*, 2022, 428, pp.116096. 10.1016/j.geoderma.2022.116096 . hal-04051589

HAL Id: hal-04051589

<https://hal.science/hal-04051589>

Submitted on 30 Mar 2023

HAL is a multi-disciplinary open access archive for the deposit and dissemination of scientific research documents, whether they are published or not. The documents may come from teaching and research institutions in France or abroad, or from public or private research centers.

L'archive ouverte pluridisciplinaire **HAL**, est destinée au dépôt et à la diffusion de documents scientifiques de niveau recherche, publiés ou non, émanant des établissements d'enseignement et de recherche français ou étrangers, des laboratoires publics ou privés.

Soil crusting: new insight from synchrotron 2D micro X-ray diffraction mapping of clay-particle orientation and mineralogy

Vincent Geoffroy¹, Baptiste Dazas¹, Eric Ferrage¹, Felisa Berenguer², Céline Boissard¹, Laurent J.
Michot³, Folkert van Oort⁴, Emmanuel Tertre¹, Fabien Hubert^{1,*}

¹ IC2MP, Equipe HydrASA, UMR 7285 CNRS/Université de Poitiers, 86073 Poitiers, France.

² Synchrotron SOLEIL, L'Orme des Merisiers, Saint-Aubin, BP48, 91192 Gif-sur-Yvette, France.

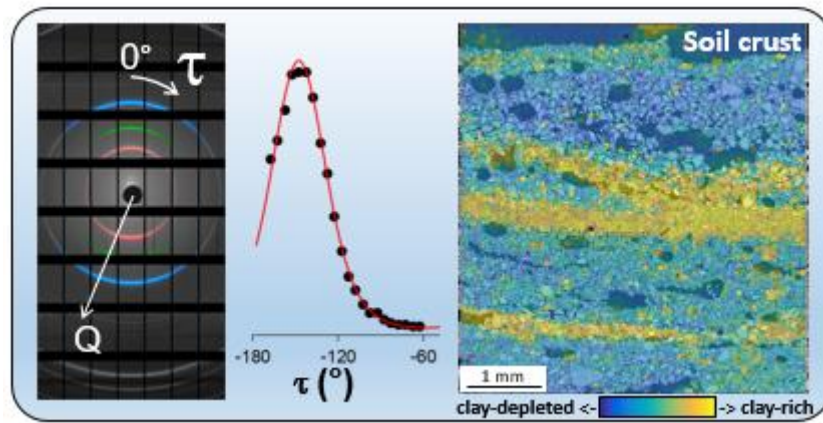
³ Phenix CNRS-Sorbonne Université UMR 8234, 4 place Jussieu case courrier 51, 75005 Paris, France.

⁴ Université Paris-Saclay, INRAE, AgroParisTech, UMR 1402 ECOSYS, 78026, Versailles Cedex, France.

*E-mail address of the corresponding author:

Fabien Hubert: fabien.hubert@univ-poitiers.fr

17 GRAPHICAL ABSTRACT



18

19

ABSTRACT

Our understanding of soil crusting and its detrimental consequences is mainly based on the analysis of morphological changes occurring at the soil surface. Such changes are usually assessed at spatial scales ranging from a few millimeters to that of the field. The inner-reorganisation within the topsoil during soil crusting primarily involves the redistribution of clay particles. Their mineralogy and arrangement remain however delicate to determine by the sole use of microscope observations. To overcome these limitations, we developed an innovative methodology based on synchrotron 2D micro X-ray diffraction (2D- μ XRD) to map relevant parameters related to the organisation of all types of soil clay minerals, i.e. relative diffracted intensities, degree of preferential orientation, mean deviation angle from the surface. Our methodological strategy was first validated on a laboratory-made model sample, composed of various pure clay phases with clear preferential orientations. Then, a vertical section of soil crust from long-term bare fallow (LTBF) experiment of the France's National Research Institute for Agriculture, Food and Environment (INRAE, Versailles, France) was studied. Micromorphological features of the soil crust were first described by using conventional scanning electron microscopy. Synchrotron 2D- μ XRD analyses were then successfully applied on the same region of interest. The in-depth analysis provided by the synchrotron 2D- μ XRD approach revealed the presence of clay microlayers that were not observed on SEM images. Additionally, clay mineralogy as well as preferred clay-particle orientation and overall alignment highlighted specific quantitative structural signatures. These signatures involved the discrimination between clay microlayers associated to the settling of clay particles in microdepressions and clayey microaggregates resulting from transportation of pre-existing soil crusts. This new technique has led to re-interpretation of the deposition mechanisms in the natural soil investigated here and opens wide perspectives for in-depth detailed characterization of clay mineralogy in soil crusts.

KEYWORDS

soil crust, synchrotron 2D- μ XRD, clay minerals, preferred particle orientation

1. INTRODUCTION

Soil crusting ranks as a major cause of soil degradation by restricting seedling emergence and triggering soil erosion (Awadhwai and Thierstein, 1985; Lal, 2001). The detrimental consequences of soil crusting are surface hardening, flattening, reduction of downward water transfer and concomitant runoff enhancement (Williams et al., 2018). Such degradation of the topsoil surface results from the breakdown of aggregates into finer fragments and/or individual particles caused by the impact of raindrops. These fine fragments are, in turn, redistributed by rainfall and/or runoff within the first millimetres depth (Bresson and Valentin, 1993). The resulting reorganization of the topsoil surface allows to directly monitor soil behaviour according to its intrinsic features (granulometry, mineral and organic constituents, physico-chemistry, topography), in response to seasonal conditions (frequency and intensity of rainfall, water content status, plant cover).

Our understanding of soil crusting and their detrimental consequences is mainly based on the analysis of morphological changes occurring at the soil surface. Such changes are usually assessed at spatial scales ranging from a few millimeters to that of the field (Williams et al., 2018). In particular, studies of soil crusts by optical microscopy have considerably improved our knowledge on pathways of soil crust formation. They have also led to propose conceptual models of crust development and classifications based on micromorphological expressions of soil crusts (Valentin and Bresson, 1992; Williams et al., 2018). Taking advantage of the higher spatial resolution provided by scanning electron microscopy (SEM), notable progress was achieved in the description of the nature and morphology of soil crusts, especially for thin layered structures (Arshad and Mermut, 1988; Chen et al., 1980; Onofriok and Singer, 1984; Wakindiki and Ben-Hur, 2002). However, this information remains restricted to morphological criteria, since the reorganisation of the topsoil surface mainly involves a redistribution of clay particles, most of which are, by far, too small (typically $< 2 \mu\text{m}$) to be identified by optical and Scanning Electron Microscopy (SEM) techniques. In addition, although orientational features of clay platelets are usually considered as markers of either the transport processes or the development stage

of soil crusting (Bresson and Boiffin, 1990; Ferry and Olsen, 1975), quantification of such preferential orientation is still lacking.

These limitations were successfully overcome on rocks (i.e. sedimentary and metamorphic rocks; Wenk et al. (2010)) and more recently on mud deposits formed under surface conditions (Wenk and Vasin, 2017). These authors used synchrotron X-ray diffraction with a 2D detector (2D-XRD) and provided simultaneous information on clay mineralogy and their orientational features. Although particularly efficient, this approach was applied for bulk characterization over several cubic millimeters of sample volume, thus not allowing for any mapping of micrometer-sized structures. More recently, synchrotron micro X-ray diffraction using a flat bi-dimensional detector (2D- μ XRD) and a higher spatial resolution of 60 μm^2 was performed on clay coatings from translocation laboratory experiments on clay depleted eluvial E-horizons of Luvisols (Manté et al., 2020). These authors demonstrated that clay mineralogical maps can be obtained from soil samples, although the geometry used did not allow providing a quantitative description of preferred orientation of clay particles. As far as clay particle orientation is concerned, Dabat et al. (2019) recently proposed a reference orientation distribution function for clay minerals potentially relevant to quantify their preferred orientation from laboratory 2D-XRD measurements on soils. Nonetheless, the applicability and interest of this approach for mapping clay particle organisation in real soil samples remains to be demonstrated.

The aim of the present work is thus to show that synchrotron 2D- μ XRD mapping is able to provide new insight on the mineralogy and orientation degree of clay particles in the framework of the soil crusting process. We developed an innovative strategy for mapping key parameters that describe the organisation of each type of clay mineral (i.e. relative diffracted intensities, degree of preferential orientation, and mean deviation angle from the surface) using synchrotron 2D- μ XRD measurements. Our methodology was first assessed on a model laboratory-made sample composed by pure clay phases. Then, micromorphological features of soil crust were studied on an in-situ surface sample from a long-term bare fallow soil. Based on the key features of clay particles provided by synchrotron 2D- μ XRD mapping analysis, new findings on formation stages of the soil crust were unraveled.

2. MATERIELS & METHODS

2.1. Materials

2.1.1. Topsoil surface sample from LTBF experiment of INRAE Versailles

The studied topsoil surface sample was collected at LTBF experiment of INRAE Versailles set up in 1928 to study the effect of various fertilizers or physico-chemical contexts on soil properties (Van Oort et al., 2018). The soil is a silt-loam textured Haplic Luvisol (WRB, 2015) developed in loess, representative of cultivated soils in North-Western Europe. The experimental site (16 × 20 m) is constituted by 42 plots of 2 × 2.5 m. It includes 16 duplicate plots receiving different chemical treatments (organic, phosphate, potassium and nitrogen fertilizers, neutral salts and basic amendments) and 10 reference plots without any inputs. The plots are kept vegetation-free and dug by spade twice a year. Among the different treatments, plot #37 that has been amended with KCl fertilizer for the past 85 years was chosen. Its physicochemical conditions dominated by a monovalent potassium cation, currently accounting for more than one third of the cation exchange capacity (van Oort et al., 2022) associated to its low amount of organic matter (7.5 g/kg of total organic carbon) resulted in a high susceptibility to physical crust formation. In 2014, the surface horizon of the KCl plot had a clay fraction (<2 µm) content of 15.8% (van Oort et al., 2022) with a complex clay mineralogy composed by kaolinite, chlorite, illite/micas, and dominated by illitic-rich interstratified illite-smectite clay minerals (Pernes-Debuyser et al., 2003). The fine silt fraction (2-20 µm) represents 58 % of the sample mass and also contains significant amounts of clay minerals, mainly chlorite, micas, and to a lesser extent, kaolinite (van Oort et al., 2022).

An undisturbed topsoil surface sample (80 mm × 80 mm × 80 mm depth) was collected in May 2014, at the end of the winter, accumulating climatic events since October 2013. The sample was then air-dried for several months, oven-dried at 40°C for 2 weeks and impregnated under vacuum with a polyester resin diluted to 33% by volume with a styrene monomer (Bruand et al., 1996). After resin polymerization, a slab perpendicular to the topsoil surface 30 mm width × 45 mm height × 1 mm thick was prepared and polished on one face for Scanning Electron Microscopy (SEM) analyses. 1 mm

diameter holes were drilled around the edge of the slab at 10 mm intervals to facilitate localization of the zones of interest between SEM and synchrotron analyses.

2.1.2. Model laboratory-made sample composed by pure clay phases

The model laboratory-made sample by pure clay phases was investigated to first assess the reliability of the approach developed for mapping clay particles organization on natural samples. The sample was selected among the model clay samples from the study of Dabat et al. (2019) because of its clay mineralogy (kaolinite, mica and vermiculite) close to the natural topsoil sample one and the variable anisotropy degree in particle orientation of constitutive single minerals deposits. The preparation procedure, detailed in Dabat et al. (2019), can be summed up as follows. After dispersion of clay particles in water by sonication, a single mineral deposit was obtained by horizontal centrifugation runs directly performed in a cylindrical sample holder under gravitational fields ranging from 4 500 to 18 000 $\times g$ (Centrifuge Avanti J 301, rotor JS-24.38 from Beckman Coulter®). Seven different deposits few millimeters thick were successively settled and the model clay sample is then composed from bottom to top by mica, kaolinite (2 deposits), mica (2 deposits), kaolinite and vermiculite (Fig. 1). The sample was then oven dried at 60°C, placed under primary vacuum to remove residual water and impregnated with Methyl Methacrylate containing benzoyl peroxide (BPO) as a thermal initiator (BPO/MMA ratio of 0.5 wt.%, (Sammaljärvi et al., 2012)) for 14 days. After resin polymerization in a 55 °C bath for 48h, the sample was sawed vertically (perpendicular to the settling direction), and a slab of 6 mm width \times 12 mm height \times ~500 μm thickness was obtained by polishing.

2.2. Methods

2.2.1. Scanning Electron Microscopy mapping

Micromorphological observations of the topsoil surface were obtained using SEM imaging in back-scattered electron mode (BSE). As the grey levels on BSE images are indicative of the atomic numbers of local elements, the discrimination between clay rich zones, silicate grains (quartz, feldspars) and pores is made easier. The SEM BSE map was obtained using an JEOL-JSM-IT500LV SEM equipped with a segmented solid state BSE detector. The polished face of the topsoil section was coated with carbon to prevent charging and the SEM BSE map was acquired on the top half part of the face, i.e. 24 mm width × 14 mm height. The automatic procedure provided by JEOL SMILE VIEW™ Lab software was used to acquire and reconstruct the SEM BSE map, which corresponds to a mosaic of 414 images. Each image was acquired at a magnitude of 130 (spatial resolution of 0.8 μm/pixel) using a working distance of 11 mm, a frame time of 10 s under an accelerating voltage of 15 kV and a probe current of 1 nA.

2.2.2. Synchrotron 2D-μXRD measurements

The experiment took place on the CRISTAL beamline at synchrotron Source Optimisée de Lumière d'Énergie Intermédiaire du LURE (SOLEIL), the French national synchrotron facility. Localized 2D-μXRD measurements, in a transmission setup, were acquired using a wavelength (λ) of 0.67055 Å selected by a Si(111) double crystal monochromator. Micro-focusing of the beam was set to 65 × 65 μm². The intensity was collected by an X-ray Pixel Array Detector (XPAD 3.2). Such detector is built from 8 modules of 7 chips each for a total resolution of 560×960 pixels. A single chip contains 120×80 pixels, each individual pixel measuring 130×130 μm, except for the first and last columns of the chip, which have a 2.5 times larger size. The detector was protected from the incident beam by a self-supported lead beam-stop. The detector is flat and perpendicular to the incident wavevector (\vec{k}_0) whose modulus is $2\pi/\lambda$. Every detector pixel encounters a scattered wavevector (\vec{k}_f) defining a

scattering angle (φ) between \vec{k}_0 and \vec{k}_f . The reciprocal length (in \AA^{-1}) is thus expressed thanks to the scattering vector modulus (Q) as:

$$Q = |\vec{k}_f - \vec{k}_0| = \frac{4\pi}{\lambda} \sin\left(\frac{\varphi}{2}\right) = \frac{2\pi}{d} \quad (1)$$

where d is the interplane distance. Samples were placed at 383.5 mm from the detector to optimize the resolution and get complete uncropped diffraction rings of every clay mineral. The model laboratory-made sample was mapped by carrying out automatic acquisition of 2D- μ XRD patterns according to a grid of 2.925 by 7.800 mm, regularly spaced by 0.065mm with a counting time of 0.2s per point. Similarly, soil maps were recorded with a grid of 4.875 by 4.550 mm, regularly spaced by 0.065mm with a higher counting time of 5s per points to ensure sufficient signal.

2.2.3. 2D- μ XRD raw data pre-treatment workflow

On-site generated Nexus files were handled using Matlab software. All processing steps needed in data treatment and later analysis, were thus managed through a new Matlab script made by the authors.

2.2.3.1. Detector correction

Raw 2D- μ XRD scans require specific processing related to both acquisition environment and sample nature. The very first correction carried out on the data concerns the removal of dead, inefficient or unreliable pixels. Thus, abnormally high, negative or zero intensity pixels positions were turned into an unrepresentable data type, also known as Not a Number (NaN), directly in the 2D- μ XRD scans. Such data type could be ignored in calculations, therefore pathological pixels did not affect calculations in any way.

The specific tiling design of the XPAD detector imposes a correction in order to remap the recorded diffracted intensities to an uncropped geometry. The 3640 μm (These Emmanuel WENGER: <https://hal.univ-lorraine.fr/tel-01751625>) blank area between each module was compensated by adding 28 extra horizontal rows of NaN pixels after each module. In addition, the chips at the module

edge are 2.5 times larger. A 5 pixels NaN vertical column was thus inserted after each chip replacing its first and last pixel leading to an actual displacement of 3 pixels. Due too poor signal and defective pixels in the vicinity of modules edges existing pixels, prior and after the extra added lines and columns were switched to NaN. These corrections bring the final undistorted image size to 1156 x 578 pixels.

2.2.3.2. Correction from resin and air

The polymerized resin (polyester or Methyl Methacrylate resins) holding the sample together generates an undesired scattering signal that raises the background of the whole patterns. 2D-μXRD acquisitions of pure resin slices (thickness: 1mm), with acquisition protocols identical to their sample counterpart, were then performed to address this issue. Averaged resins 2D-μXRD scans were generated from 9 points targeted randomly at the pure slices.

To lessen the resin contribution, a normalization was carried out on each 2D-μXRD such as:

$$2D\mu XRD_{Sample\ resin\ Removed} = 2D\mu XRD_{Sample} - (2D\mu XRD_{Resin} * F) \quad (2)$$

The final treated image ($2D\mu XRD_{Sample\ resin\ removed}$) is calculated from the raw pattern ($2D\mu XRD_{Sample}$) from which a weighted contribution (F) of pure resin $2D\mu XRD_{Resin}$ is removed.

This ponderation is calculated according to:

$$F = \frac{1}{n_i n_j} \sum_{i=30}^{70} \sum_{j=600}^{630} \frac{2D\mu XRD_{Sample\ ij}}{2D\mu XRD_{Resin\ ij}} \quad (3)$$

with i and j the respective horizontal and vertical positions of the pixels in the image and n the number of corresponding pixels. F thus represents the average intensity ratio factor between an area of 30 X 40 pixels² devoid of diffraction rings, on the sample diffraction pattern and this same area on the average resin 2D-μXRD pattern. The computed F values are stored for each diffraction spot of a map allowing to assess resin treatment correctness as well as to gain insight on the relative proportion of resin present in the diffracted spot. This factor will theoretically reach a value of one for a pure resin spot (with a thickness similar to resin standard) in the mineral sample and decrease towards zero for

any mineral/resin mixture with a higher absorption coefficient. Any value above one would simply be linked to a diffraction spot being pure resin, thinner than the 1 mm resin standard or simply to air.

2.2.4. Data extraction

Mapping the clay mineralogy and anisotropy in the sample relies on a detailed analysis of the nature and intensity of the crystalline clay phases from the $I(Q, \tau)$ distribution of individual 2D- μ XRD images. The detection procedure of diffraction peaks associated to each clay phase is simplified on an averaged 1D-XRD pattern $I^{av.}(Q)$ over all individual scans of the samples. As illustrated in Fig. 2 for the laboratory-made sample, an average 2D- μ XRD image $I^{av.}(Q, \tau)$ is first calculated (Fig. 2a) and a mean 1D- μ XRD pattern $I^{av.}(Q)$ is then extracted by integrating the image with a 0.005 \AA^{-1} Q -step across the entire azimuthal angle τ (Fig. 2b). The obtained $I^{av.}(Q)$ pattern provides the global sample mineralogy thus allowing minerals boundaries selections (Fig. 2b) covering the Q -range associated to each mineral. For this model clay sample, vermiculite (in red), mica (in green), and kaolinite (in blue), are selected based on their classical 001 reflection at 14.20, 10.00, and 7.14 \AA , respectively (Fig. 2b). For these three minerals phases, the integrated intensities values $I_i(\tau)$ (with i =vermiculite, mica, or kaolinite) are extracted over 360° of τ angular range on the detector with a step of 8° for each individual 2D- μ XRD scan considering a Q -range selection from 0.371 to 0.503 \AA^{-1} , 0.589 to 0.650 \AA^{-1} , and 0.806 to 0.938 \AA^{-1} , respectively (Figs. 2 and 3). A linear background contribution taken at the vicinity of the high and low boundaries of each minerals was subtracted. The intensity modulation of the extracted function displays two symmetric maxima at $\pm\pi$ along the diffraction ring (Fig. 3), associated to the development of preferred orientation in clay particle arrangement. The intensity maxima represent the symmetry axis of the transverse isotropic organisation repeatedly demonstrated for clay systems (Dabat et al., 2019; Dabat et al., 2020; Wenk et al., 2010). In the framework of the $\tau = \theta$ approximation (Dabat et al., 2019) the $I_i(\tau)$ function can be directly linked to the orientation distribution function (ODF) $f_i(\theta)$. The ODF quantifies the amount of particle whose normal forms an angle θ with the main symmetry axis of the clay medium and is expressed as:

$$I_i(\tau) = k' \cdot f_i(\theta + \Delta_i) \quad (4)$$

where k' is a normalisation constant and Δ_i the deviation angle between the detector reference and the symmetry axis in preferred orientation of clay particles (Fig. 3). The ODF is defined by the following constraints (Dabat et al., 2019; Labarthet et al., 2000):

$$f_i(\theta) \geq 0 \quad (5)$$

$$f_i(\theta) = f(\pi - \theta) \quad (6)$$

$$\int_0^\pi f_i(\theta) \sin(\theta) d\theta = 1 \quad (7)$$

To overcome the lack of experimental data points in the accessible τ -range, related to the tilling of the 2D detector (solid circles; Fig. 3b), data treatment of experimental $I_i(\tau)$ functions involves and automatized fitting procedure of intensities by the generalised orientation distribution function proposed by Dabat et al. (2019) (solid red line; Fig. 3b). This function is based on the maximum-entropy theory and takes the form of:

$$I_i(\tau) = k'' \exp[\lambda_2 P_2(\cos(\theta + \Delta_i)) + 0.005(\lambda_2)^5 P_4(\cos(\theta + \Delta_i))] \quad (8)$$

where λ_2 is the spreading parameter of the ODF and where k'' a normalisation constant. The entities $P_2(\cos\theta)$ and $P_4(\cos\theta)$ stand for the 2nd and 4th rank Legendre polynomials, respectively, expressed as:

$$P_2(\cos\theta) = \frac{1}{2}(3\cos^2\theta - 1) \quad (9)$$

$$P_4(\cos\theta) = \frac{1}{8}(35\cos^4\theta - 30\cos^2\theta + 3) \quad (10)$$

The convergence of the automatized fitting procedure of experimental $I_i(\tau)$ intensities is favoured by the removal of the values exceeding three times the interquartile range above the third quartile. By doing so, high intensity spots linked to coarse grain diffraction can be filtered. The extraction of the ODF function $f_i(\theta)$ full shape by combining Eqs. (4) and (8) allows eliminating the tilling of the detector and the full range of τ values can then advantageously be used for calculating the order parameter $\langle P_2 \rangle_i$ and the number of particles N_i of each clay mineral i in each 2D- μ XRD

scan. The order parameter $\langle P_2 \rangle_i$, characterizing the degree in preferred orientation of the mineral i , is calculated as:

$$\langle P_2 \rangle_i = \int_0^\pi P_2(\cos\theta) \cdot f_i(\theta) \sin(\theta) d\theta \quad (11)$$

This parameter, also known as the Hermans or nematic order parameter (Chaikin and Lubensky, 1995; Hermans and Platzek, 1939), takes the value of 0 for a random organisation of particles and 1 for perfectly aligned particles along the symmetry axis.

In order to describe the evolution of clay mineralogy, the parameter N_i relative to the number of particles of a clay mineral i in each 2D- μ XRD pattern was chosen and calculated as:

$$N_i = \int_0^\pi k' \cdot f_i(\theta) \sin(\theta) d\theta \quad (12)$$

This quantity was preferred over the intensity parameter because any change in the overall 001 reflection intensity of a mineral between two 2D- μ XRD scans can be related to both the proportion of the mineral and the degree in preferred orientation. As indicated in Eq. (12), calculation of N_i parameter is thus done by correcting the 001 reflection intensities by the term $\sin(\theta)$, so that the change in intensity from one pixel to the other in the map is solely related to a variation in the mineral proportion (Perdigon-Aller et al., 2005). Note that the quantities N_i are only indicative of the variation of the clay mineral content among different pixels from the map. This entity cannot be used in any case as an absolute value, and does not provide a comparison between different minerals that would require accounting for the change in structure factor of the mineral i (Moore and Reynolds, 1997).

As far as the natural soil sample is concerned, additional mineralogical quantities can be extracted from 2D- μ XRD map, especially concerning the mapping of whole clay minerals using hk bands and quartz. To do so, Q -boundaries were set at 1.399 and 1.458 \AA^{-1} as well as 1.876 and 1.945 \AA^{-1} , for hk bands and quartz, respectively (Table S1). For these XRD reflections, calculation of N parameters according to ODF calculations using Eq. (8) cannot be performed and the maps were thus generated from a direct integration of experimental intensities $I(Q, \tau)$ as:

$$I_j = \int_0^{2\pi} \left[\int_{Q_{min}^j}^{Q_{max}^j} I(Q, \tau) dQ \right] d\tau \quad (13)$$

Where j corresponds to the hk bands or quartz entities. Q_{min}^j and Q_{max}^j stand for the minimum and maximum of Q -boundaries of the associated j entities, respectively.

3. RESULTS

3.1. Model laboratory-made sample composed by pure clay phases

3.1.1. Parameters mapping and sensitivity of the method to structural features

The methodological strategy used for mapping the clay mineralogy and anisotropy in clay particles orientation is assessed for this sample based on the mineral detection (i.e., vermiculite, mica, and kaolinite) through 1D- μ XRD pattern $I^{av.}(Q)$ (Fig. 2) and experimental $I_i(\tau)$ functions (Fig. 3).

In Fig. 4, the values calculated for the N_i , $\langle P_2 \rangle_i$, and Δ_i parameters (i = vermiculite, mica, and kaolinite from left to right) for all 2D- μ XRD scans are transformed into colour-coded maps. The maps can be compared to the original photograph of the sample (Fig. 1) and well illustrate the positions of the different minerals within the model sample (Fig. 4). In the following, the obtained maps are used to assess the sensitivity of the method to highlight specific structural features that can help to decipher the deposition process of clay particles during sedimentation. To do so, the different sub-beds are segmented into bottom, middle, and top sub-beds according to the image mask reported in Fig. S1.

3.1.2.1. Sensitivity to sedimentation events

The obtained parameter maps provide clear distinction between the different beds as well as sub-beddings (Fig. 4), i.e., when the mineral is deposited in two successive steps during sedimentation using the same preparation conditions (Fig. 1). For vermiculite, the single sedimentation process leads to the presence of a single bed with noticeable structure evolution within. Firstly, the bottom part of the bed is shown to be denser as seen by higher values for N_V parameters (Fig. 4a) and lower resin content (Fig. 1c). Secondly, the increased particle density is accompanied by an increasing trend of $\langle P_2 \rangle_V$ values (Fig. 4b). Such a correlation between density and preferential orientation was already reported for lamellar particles (Ferrage et al., 2015; Voltolini et al., 2008). For mica and kaolinite clay

minerals, the increase of N_i and $\langle P_2 \rangle_i$ values at the lower part of the sub-beds for these two minerals is also clearly visible, likely indicating that the proposed methods is fully capable in principle of evidencing high-frequency sedimentation events. Note that, the limit between two sub-beds and associated structural discontinuity can be responsible for the detachment of the two units during drying. This is the case here between the two adjacent sub-beds of mica, with a full separation of the layers as revealed by the resin map (Fig. 1c).

3.1.2.2. Sensitivity to deposition conditions

The calculated parameters can also be used to assess the efficiency of the method to detect changes in the experimental conditions used for particle disposition (Figs. 1b and 4). For the two adjacent sub-beds of mica or kaolinite prepared using the same sedimentation conditions (Fig. 1b), the structural properties of the clay particles are remarkably similar in terms of particle density and orientation (maps and histograms in Figs. 4a and 4b). The situation differs when comparing for kaolinite the top bed and the two other adjacent sub-beds. The top bed appears to be indeed denser and with an increased particle orientation (histogram in Fig. 4b). This change can be directly assigned to the preparation conditions and to the higher concentration of the kaolinite dispersion considered (i.e., 50 g.L⁻¹; Fig. 1b). For the top bed, the lower gravitational field applied can be considering as sufficient to allow the particles to separate in this concentrated dispersion and lying flat on the existing bed (Figs. 4a and 4b). For the middle and bottom sub-beds the high velocity of sedimentation is likely to hamper the sedimentation process, thus leading to the obtained structures with aggregates of less oriented particles (Figs. 4a and 4b). In the case of mica, the lower dispersion concentrations (i.e., 25 g.L⁻¹; Fig. 1b) is likely responsible of the more limited influence of the strength of the applied gravitational field, all sub-beds showing indeed similar structural features (Figs. 4a and 4b).

3.1.2.3. Sensitivity to topographical effects

In addition to the investigation of the different sedimentation events, analysis of parameter maps allows analyzing the impact of topography on the deposition of particles. For instance, perturbation of sedimentation is shown to impact all clay mineral phases at the interface of the

dispersion and the tube (right part of the maps; Fig. 4). Such a perturbation induces an overall decrease in $\langle P_2 \rangle$ values and minerals intensities (or an increase in porosity) as well as an increase in Δ values resulting from this wall-effect (Figs. 4b and 4c).

3.2. Topsoil surface of the KCl plot from LTBF experiment of INRAE Versailles

3.2.1. Micromorphological features of the soil crust from BSE SEM map

Observations from the BSE MEB map (Fig. 5) indicate that the topsoil surface of the KCl plot exhibits micromorphological features typical of an advanced stage of physical crust formation. This advanced stage, previously described by Bresson and Boiffin (1990) on the same LTBF experiment, corresponds to the development of a structural crust covered by a sedimentary crust (Fig. 5a). The structural crust is characterized by a continuous dense fabric (without separated aggregates) dominated by silts in which sand grains surrounded by clay particles are most often randomly distributed or, to a lesser extent, with limited segregation. The macropores (hundreds of micrometres sizes) are essentially elongated vughs parallel to the topsoil surface whereas vesicular voids are also present. Based on the interpretation of Bresson and Boiffin (1990) this specific inner-organisation of the structural crust (vughy structure according to Bullock et al. (1985)) results from the gradual coalescence of the initial aggregates by raindrop compaction under plastic conditions. The formation of this structural crust most often corresponds to the last stage of development before the formation of a sedimentary crust (Williams et al., 2018). In the present case, the overlying sedimentary crust is rather thin (between 3 and 4 mm in thickness; Fig. 5a) and the morphology of the macroporosity differs from the structural crust by the dominance of individual or coalescing vesicular voids. In addition, the inner-structure is much more complex and formed by successive deposits of several microlayers or microbeds parallel the topsoil surface.

A region of interest (ROI) at a 5 mm depth from the topsoil surface and 4.5 mm in width (Fig. 5b), selected for synchrotron μ XRD-mapping, is first described below according to classical micromorphological descriptors. As illustrated on this BSE SEM image, the ROI can be divided into four

successive zones (numbered from 1 to 4 from the bottom of the BSE SEM map and separated by dashed solid lines; Fig. 5b). Zone 1 corresponds to the top part of the structural crust. The clear separation with zone 2 and the bottom of the sedimentary crust is marked by a very thin clayey microlayer less than 150 μm thick that includes coarse quartz grains (Figs. 5b and 5c). Such deposit of a continuous clayey microlayer was previously described as occurring in small pocket-like depressions and resulting from short-distance transport of particles by runoff under turbulent and muddy flow process (Bresson and Valentin, 1993). The overlying part of zone 2 is characterized by the successive deposits of well sorted microlayers exhibiting a clear fining-upward textural gradient (Figs. 5b and 5d), i.e., from sands at the bottom to silts/clays at the top. Such type of deposit is also interpreted as related to a runoff-sedimentation regime but in a more laminar flow allowing the sorting of microlayers and the gradual settling from coarse to fine particles (Valentin and Bresson, 1992). The transition between zones 2 and 3 is marked by the deposition of a poorly-sorted micro-beds including coarse quartz grains overlaying the silts/clays microlayer localised at the top of zone 2 (Figs. 5b and 5d). Zone 3 also includes some microaggregates on its top part (Figs. 5b and 5e) that can be partially disaggregated (e.g., on the left part of Fig. 5e). Some of the microaggregates seem to be enriched in fine particles. Limited particle size sorting is commonly assigned to a deposition under turbulent flow process as for the bottom part of the sedimentary crust while presence of microaggregates on the top part most likely suggests a higher flow velocity or they were deposited by afterflow (Mücher and De Ploey, 1977). Separation between zones 3 and 4 (dashed line on Fig. 5b) is based on the deposition of coarser sand grains surrounded by silt/clay particles on partially disaggregated microaggregates. Finally, zone 4 corresponds to the last deposit and exhibits a higher macroporosity compared to the underlying ones. The inner-structure is mainly dominated by poorly-sorted micro-bed of sand grains (again surrounded by silt/clay particles) and covering a well sorted microlayer composed by silts/clays. This last deposit, with a partial upward textural gradient, could be interpreted as formed in between turbulent and laminar flow conditions, depending on runoff and splash conditions (Mücher and De Ploey, 1977; Valentin and Bresson, 1992).

3.2.2. Soil crust micromorphology characterization from the 2D- μ XRD map

The mapping of clay mineralogy and anisotropy in clay particles orientation of the soil crust was obtained using the 2D- μ XRD methodological strategy validated on the model laboratory-made sample. Detection of minerals nature and Q -boundaries is first achieved based on the $I^{av.}(Q)$ pattern of the topsoil sample (Fig. 6; Table S1) exhibiting the 00ℓ reflections of chlorite (001 at 0.44 \AA^{-1} , 002 at 0.89 \AA^{-1} , and 003 at 1.32 \AA^{-1}), illite/micas (001 at 0.62 \AA^{-1} , 002 at 1.25 \AA^{-1} , and 003 at 1.87 \AA^{-1}), and kaolinite (001 at 0.87 \AA^{-1} and 002 at 1.75 \AA^{-1}) with their common hk bands ($02\ell - 11\ell$ at $\sim 1.41 \text{ \AA}^{-1}$).

Note that the clay mineralogy is in agreement with that described by van Oort et al. (2022) for the silt fraction but differs from that proposed by Pernes-Debuyser et al. (2003) for the clay fraction, in which interstratified illite-smectite phases are dominant. This can be assigned to the KCl treatment that leads to an evolution of the interstratified illite-smectite phases towards illite like phases due to the collapse of the interlayer space of smectite layers resulting from potassium exchange. In addition, the very intense diffraction peak at $\sim 1.89 \text{ \AA}^{-1}$ indicates that quartz is also a dominant mineral phase. The several remaining relatively intense diffraction peaks correspond to feldspars, i.e. microcline and orthoclase (Fig. 6).

A first micromorphological information based on 2D- μ XRD map can be achieved from the mapping of whole clay minerals using hk bands and quartz intensities using Eq. (13) (Figs. 6, 7a and 7b). To do so, Q -boundaries were set at 1.399 and 1.458 \AA^{-1} as well as 1.876 and 1.945 \AA^{-1} , for hk bands and quartz, respectively (Table S1). Superimposition of the deposition zones limits from Fig. 5b on I_{hk} map (Fig. 7a) reveals a high heterogeneity of the clay phases spatial distribution in agreement with sequential depositional events. The thin clayey microlayer at the bottom of the sedimentary crust, observed by SEM analyses, is confirmed on 2D- μ XRD maps by the increase of I_{hk} values (clay microlayer A at the transition between zone 1 and 2 on Figs. 7a and 7c). The transition between the denser structural crust and the sedimentary crust, where the thin clayey layer is located, is also highlighted by the clear contrast on the resin map (Fig. 7d). Noteworthy, while the I_{hk} map confirms

the clay-rich composition of microaggregates in zone 3 (clay microlayer C; Fig. 7c), the method reveals the presence of two additional thin clay microlayers (clay microlayer B and D; Fig. 7c) that cannot be detected from SEM analyses (Figs. 5b and 5d).

Beneficiating from the efficiency of the 2D- μ XRD method, additional insights can be obtained regarding clay mineralogy and clay particles preferred orientation within the soil crust and associated to each clay-rich microlayer (Fig. 8). Note that the efficiency of the method to discriminate the 001 reflection of kaolinite from the 002 reflection of chlorite was successfully assessed by the similar maps obtained using either the 001 or 002 reflections of chlorite (Fig. S2) as well as the clear differences between 2D parameter maps obtained for kaolinite or chlorite (Fig. 8). The obtained 2D parameters maps for clay minerals (Fig. 8) are discussed below and used to draw a general scheme of the successive events at the origin of the soil crust formation.

4. DISCUSSION

The analysis of the model clay samples has proven the efficiency of the methodological strategy developed for mapping mineral density and orientation parameters (i.e., $\langle P_2 \rangle$ and Δ) thus allowing obtaining key information about sedimentation processes (number of events, particle sizing, and topographic impact). In that regard, this approach can be used to deepen the classical micromorphological description based on SEM observations for clay microlayers encountered in complex soil samples (Chen et al., 1980; Onofiok and Singer, 1984). Indeed, according to conventional micromorphological descriptors, the successive microlayers/micro-beds of the complex sedimentary crust can be interpreted in terms of runoff depositional crust as suggested by Valentin and Bresson (1992). Following such an interpretation, the depositional events mainly take the form of unsorted clay-rich deposits (Fig. 5c) or microlayers with a fining-upward textural gradient (Fig. 5d), according to the turbulent or laminar hydrodynamic conditions during particle sedimentation, respectively.

Although such SEM-based observations lead to the description of the main successive depositional processes of particles, analysis of 2D- μ XRD map can be used to get additional insights into

the mechanistic processes of soil crust formation. Clay microlayers A and B indeed display similar textural features for illite/mica and kaolinite (Fig. 8). This concerns the preferred orientation (average $\langle P_2 \rangle$ values of ~ 0.18 and ~ 0.10 for illite/mica and kaolinite, respectively; Fig. 8b) as well as a clear overall alignment of particles parallel to the soil surface (low Δ parameter for both minerals; Fig. 8c). Such similarities likely plead for similar depositional process of clay accumulation by settling as commonly reported for skin seal (Arshad and Mermut, 1988; Chen et al., 1980; Norton, 1987). Contrastingly, analysis of chlorite 2D map reveals higher contents and preferred orientation of chlorite particles in microlayer B compared to microlayer A (average $\langle P_2 \rangle_c$ value of ~ 0.08 and ~ 0.02 for microlayers B and A, respectively; Fig. 8b). Accordingly, and in agreement with SEM observations, zone 1 corresponds to the top part of the structural crust, likely clay-depleted by first runoff washing (Mücher and De Ploey, 1977). The limited content in chlorite for the clay microlayer A likely pleads for their translocation by runoff, according to their silt size (Pernes-Debuyser et al., 2003; van Oort et al., 2022). The final stage of this event thus includes clay minerals settling of finest particles (i. e. illite/mica and kaolinite; Fig. 8) onto remaining coarse quartz grains after runoff stopped, leading to oriented and flat deposition of clay particles. This two steps process (runoff washing followed by particle settling) previously proposed by Norton (1987) significantly differs from the muddy flow process interpretation of concomitant deposition of coarse grains and clays based solely on SEM observations. Concerning the deposition of zone 2 and clay microlayer B, runoff-sedimentation regime under laminar flow is validated. This corresponds to the interpretation based on SEM, complemented here by the 2D- μ XRD method. Indeed, the latter reveals (i) a first deposition of well sorted microbeds of quartz depleted in clay particles (Figs. 7a and 7b) and (ii) a final stage of deposition marked by the clay microlayer B with well oriented particles (Figs. 8). This clearly illustrates the added value of the 2D- μ XRD method for in-depth probing of crust process formation compared to surface SEM observations that may miss out such type of final clay accumulation. Presence of the clay microlayer B confirms the deposition process of quartz grains suggested by Radcliffe et al. (1991) and discards the presence of a “washing out” layer in the present case. These two clay microlayers exhibits orientation degrees in the range of those

quantified for the first time on natural samples developed under surface conditions, i. e. mud deposits (Wenk and Vasin, 2017). Compared to the average degree of preferred orientation measured for the model laboratory-made sample composed by pure clay phases (Fig. 4b), values are clearly lower. The limited preferred orientation in clay microlayers can be tentatively assigned either to the deposition of clay particles on surfaces with very high roughness constituted by coarse grains or deposition of clay particles that remain partially aggregated with silts.

Clay microlayer C at the top of zone 3 is clay-rich (Fig. 7a) and depleted in quartz (Fig. 7b). Compared to the micro-layers A and B that are continuous and made up of aligned clay particles (low delta value; Fig. 8c), microlayer C shows evidence of a specific signature of clay minerals associated to microaggregate morphology, in agreement with SEM observations (Fig. 5e). This specific structural feature can be revealed by a weaker average orientation with spotty pattern (Fig. 8b), without any specific alignment (Fig. 8c). The whole organisation of microlayer C thus matches well with that observed for deposition of aggregates in the model laboratory-made sample (Figs. 4b and 4c). In addition, 2D- μ XRD provides additional information regarding the formation of these micro-aggregates. Indeed, the local significant degree in preferred orientation ($\langle P_2 \rangle$ values up to 0.15 for illite/mica and kaolinite; Fig. 8b) as well as clay accumulation likely pleads for the presence of fragments of pre-existing depositional crust. The poor alignment of particles (Fig. 8c) is thus logically associated to the transportation of clay materials under the form of microaggregate and their deposition in micro-depressions during intense runoff (Bresson and Valentin, 1993).

The 2D- μ XRD method highlights the last depositional event in zone 4, which is characterized once again by clay accumulation under the form of the clay microlayer D (Fig. 7a). This last depositional event presents the same mineralogical and morphological features as that observed in zone 2 with sorted microlayers of quartz grains stripped of clay particles (Figs. 7a and 7b) and overlaid by a clay microlayer at the top soil surface. This clay microlayer D is continuous but with more diffuse pattern (Figs. 7a and 8a) than the previous ones and almost isotropic. Only particles of the illite/mica display a very weak orientation and an alignment (Fig. 8b and 8c). Beneficiating from the contribution of SEM

observations, the structural features of clay microlayer D revealed by 2D- μ XRD likely indicate that clay particles were clay infillings within interparticle porosity as well as meniscus-like bridges between coarser grains (Bresson and Cadot, 1992).

5. CONCLUSIONS

2D- μ XRD represents a key method for mineralogical and textural mapping on a centimeter scale field of view and at a resolution of a few tens of microns. This approach was successfully applied here to laboratory-made and natural clay-rich samples.

In the field of soil micromorphology and soil crust formation interpretation, such a method represents a key addition to SEM observations as it jointly provides mineralogical information, especially on the clay phases and their orientational features, i.e. parameters that were currently inaccessible. Moreover, the in-depth analysis provided by this technique revealed the existence of clay microlayers that were not observed by surface SEM characterization. Textural information regarding clay preferred orientation and overall alignment allowed for unambiguous re-interpretation of the SEM data regarding depositions mechanisms. Accordingly, specific structural signatures were associated to the presence of clay microlayers associated to the settling of clay particles in micro-depressions and clayey microaggregates resulting from transportation of pre-existing soil crusts.

New insights from fine quantification of particle preferred orientation associated to each clay mineral could clearly be applied to investigate in depth the influence of physical-chemistry environments on soil crusting. Indeed, the degree of preferential orientation of particles appears as a primary signature of clay deposition processes, which in turn is significantly impacted by physico-chemical conditions (i.e. particle dispersion according to clay mineralogy and particle size). Accordingly, one of the logical perspectives of this work could be to consider the different plots with different chemical treatments of the LTBF site to further investigate the role played by soils physico-chemical conditions on soil crusting. In that context, one may expect to observe clay microlayers with $\langle P_2 \rangle$ values ranging from those obtained for the KCl soil investigating here to potentially very high $\langle P_2 \rangle$

values as obtained for the laboratory-made sample in the case of soil crusting exhibiting still depositional micromorphology (Valentin and Bresson, 1992). Another logical perspective of this work could be to take advantage of the 2D- μ XRD method coupled to on-site rainfall simulator in order to deepen our understanding of the various climatic factors (i.e., rainfall, runoff, and after flow intensities,) affecting mechanisms of soil crust formation and more generally soil erosion. Last interesting outlooks could also concern the use of spatialized mineralogical and textural information of clay minerals as indicators to follow the evolution of topsoil structure in current problematics about soil conservation or restoration involving natural, cultivated, or constructed Technosols.

ACKNOWLEDGEMENTS

The results presented here are part of the PhD thesis of V.G. granted by “Région Nouvelle-Aquitaine”, University of Poitiers, France. The authors acknowledge assistance from the CRISTAL beamline of synchrotron SOLEIL for 2D- μ XRD measurements (Proposal No. 20181366-standard). The authors are grateful to Thomas Dabat for the preparation of the model sample and to Claude Laforest and Claude Veit for technical assistance. The “environmental mineralogy” platform at IC2MP is acknowledged. The authors are grateful to the CNRS interdisciplinary “défi Needs” program (Project DARIUS), the French government program “Investissements d’Avenir” (EUR INTREE, reference ANR-18-EURE-0010), and the European Union (ERDF) and “Région Nouvelle Aquitaine” for providing financial support for this study.

REFERENCES

- Arshad, M.A., Mermut, A.R., 1988. Micromorphological and Physico-chemical Characteristics of Soil Crust Types in Northwestern Alberta, Canada. *Soil Science Society of America Journal* 52(3), 724-729.
- Awadhwai, N.K., Thierstein, G.E., 1985. Soil crust and its impact on crop establishment: A review. *Soil and Tillage Research* 5(3), 289-302.
- Bresson, L.M., Boiffin, J., 1990. Morphological characterization of soil crust development stages on an experimental field. *Geoderma* 47(3), 301-325.
- Bresson, L.M., Cadot, L., 1992. Illuviation and Structural Crust Formation on Loamy Temperate Soils. *Soil Science Society of America Journal* 56(5), 1565-1570.

- Bresson, L.M., Valentin, C., 1993. Soil surface crust formation: contribution of micromorphology. In: A.J. Ringrose-Voase, G.S. Humphreys (Eds.), *Developments in Soil Science*. Elsevier, pp. 737-762.
- Bruand, A., Cousin, I., Nicoullaud, B., Duval, O., Bégon, J.C., 1996. Backscattered Electron Scanning Images of Soil Porosity for Analyzing Soil Compaction around Roots. *Soil Science Society of America Journal* 60(3), 895-901.
- Bullock, P., Fedoroff, N., Jongerius, A., 1985. *Handbook for soil thin section description*. Waine, Albrighton.
- Chaikin, P.M., Lubensky, T.C., 1995. *Principles of Condensed Matter Physics*. Cambridge University Press, Cambridge.
- Chen, Y., Tarchitzky, J., Brouwer, J., Morin, J., Banin, A., 1980. Scanning Electron Microscope Observations on Soil Crusts and their Formation. *Soil Science* 130(1).
- Dabat, T., Hubert, F., Paineau, E., Launois, P., Laforest, C., Grégoire, B., Dazas, B., Tertre, E., Delville, A., Ferrage, E., 2019. A general orientation distribution function for clay-rich media. *Nature Communications* 10(1), 5456.
- Dabat, T., Porion, P., Hubert, F., Paineau, E., Dazas, B., Grégoire, B., Tertre, E., Delville, A., Ferrage, E., 2020. Influence of preferred orientation of clay particles on the diffusion of water in kaolinite porous media at constant porosity. *Applied Clay Science* 184, 105354.
- Ferrage, E., Hubert, F., Tertre, E., Delville, A., Michot, L.J., Levitz, P., 2015. Modeling the arrangement of particles in natural swelling-clay porous media using three-dimensional packing of elliptic disks. *Physical Review E* 91(6), 062210.
- Ferry, D.M., Olsen, R.A., 1975. Orientation of Clay Particles as it Relates to Crusting of Soil. *Soil Science* 120(5).
- Hermans, P.H., Platzek, P., 1939. Beitrage zur kenntnis des deformationsmechanismus und der feinstruktur der hydratzellulose. *Kolloid-Z* 88(68).
- Labarthet, F.L., Buffeteau, T., Sourisseau, C., 2000. Orientation Distribution Functions in Uniaxial Systems Centered Perpendicularly to a Constraint Direction. *Appl. Spectrosc.* 54(5), 699-705.
- Lal, R., 2001. Soil degradation by erosion. *Land Degradation & Development* 12(6), 519-539.
- Manté, C., Borschneck, D., Mocuta, C., van den Bogaert, R., Montagne, D., Cammas, C., Cornu, S., 2020. Combining wavelets with statistical inference to map the mineralogical composition of pedological features from synchrotron X-ray diffraction data. *SN Applied Sciences* 2(7), 1265.
- Moore, D.M., Reynolds, R.C., 1997. *X-Ray Diffraction and the Identification and Analysis of Clay Minerals*. 2 ed. Oxford University Press, USA.
- Mücher, H.J., De Ploey, J., 1977. Experimental and micromorphological investigation of erosion and redeposition of loess by water. *Earth Surface Processes* 2(2-3), 117-124.
- Norton, L.D., 1987. Micromorphological study of surface seals developed under simulated rainfall. *Geoderma* 40(1), 127-140.
- Onofiok, O., Singer, M.J., 1984. Scanning Electron Microscope Studies of Surface Crusts Formed by Simulated Rainfall. *Soil Science Society of America Journal* 48(5), 1137-1143.
- Perdigon-Aller, A.C., Aston, M., Clarke, S.M., 2005. Preferred orientation in filtercakes of kaolinite. *Journal of Colloid and Interface Science* 290(1), 155-165.
- Pernes-Debuyser, A., Pernes, M., Velde, B., Tessier, D., 2003. Soil mineralogy evolution in the INRA 42 plots experiment (Versailles, France). *Clays and Clay Minerals* 51(5), 577-584.
- Radcliffe, D.E., West, L.T., Hubbard, R.K., Asmussen, L.E., 1991. Surface Sealing in Coastal Plains Loamy Sands. *Soil Science Society of America Journal* 55(1), 223-227.
- Sammaljärvi, J., Jokelainen, L., Ikonen, J., Siitari-Kauppi, M., 2012. Free radical polymerisation of MMA with thermal initiator in brick and Grimsel granodiorite. *Engineering Geology* 135-136, 52-59.
- Valentin, C., Bresson, L.M., 1992. Morphology, genesis and classification of surface crusts in loamy and sandy soils. *Geoderma* 55(3), 225-245.
- van Oort, F., Paradelo, R., Baize, D., Chenu, C., Delarue, G., Guérin, A., Proix, N., 2022. Can long-term fertilization accelerate pedogenesis? Depicting soil processes boosted by annual NPK-inputs since 1928 on bare loess Luvisol (INRAE-Versailles). *Geoderma* 416, 115808.

- Van Oort, F., Paradelo, R., Proix, N., Delarue, G., Baize, D., Monna, F., 2018. Centennial Fertilization-Induced Soil Processes Control Trace Metal Dynamics. Lessons from a Long-Term Bare Fallow Experiment. *Soil Systems* 2(2).
- Voltolini, M., Wenk, H.-R., Mondol, N.H., Bjørlykke, K., Jähren, J., 2008. Anisotropy of experimentally compressed kaolinite-illite-quartz mixtures. *GEOPHYSICS* 74(1), D13-D23.
- Wakindiki, I.I.C., Ben-Hur, M., 2002. Soil Mineralogy and Texture Effects on Crust Micromorphology, Infiltration, and Erosion. *Soil Science Society of America Journal* 66(3), 897-905.
- Wenk, H.-R., Kanitpanyacharoen, W., Voltolini, M., 2010. Preferred orientation of phyllosilicates: Comparison of fault gouge, shale and schist. *Journal of Structural Geology* 32(4), 478-489.
- Wenk, H.R., Vasin, R., 2017. PREFERRED ORIENTATION PATTERNS OF PHYLLOSILICATES IN SURFACE CLAYS. *Clays and Clay Minerals* 65(5), 329-341.
- Williams, A.J., Pagliai, M., Stoops, G., 2018. Chapter 19 - Physical and Biological Surface Crusts and Seals. In: G. Stoops, V. Marcelino, F. Mees (Eds.), *Interpretation of Micromorphological Features of Soils and Regoliths* (Second Edition). Elsevier, pp. 539-574.
- WRB, I.W.G., 2015. World Reference Base for Soil Resources 2014, Update 2015. International soil Classification System for Naming Soils and Creating Legends for Soil Maps; World Soil Resources Reports No. 106
FAO, Rome.

FIGURE CAPTIONS

Figure 1. (a) Photograph of the slice of laboratory-made sample before synchrotron analysis with the red rectangle indicating the region of interest for synchrotron analysis. (b) Concentration of the dispersion, centrifugation conditions, and particle size of the different clay phases. (c) 2D map of the resin factor F according to Eq. (3).

Figure 2. (a) Averaged 2D- μ XRD pattern $I^{av}(Q, \tau)$ and definition of scattering vector modulus Q and azimuthal angle τ on the detector for the model sample. 001 diffraction rings associated to vermiculite (V), mica (M), and kaolinite (K) are shown in red, green and blue, respectively. (b) Averaged $I^{av}(Q)$ pattern and definition of mineral boundaries for extraction of intensity $I_i(\tau)$ associated to each clay mineral i .

Figure 3. Illustration of the vermiculite orientation distribution function ($f_V(\theta)$) extraction for the model sample. (a) Selection of an individual 2D- μ XRD pattern and extraction of the intensity $I_V(\tau)$. (b) Comparison between the experimental data $I_V(\tau)$ (solid symbol) and fitted function (solid red line) according to Eq. (8). The dotted grey line represents the function $k' \cdot f_V(\theta)$. Parameter Δ_V stands for the deviation angle between the main preferred orientation axis of vermiculite particles and the detector reference. The order parameter $\langle P_2 \rangle_V$ corresponds to the degree of preferential orientation of vermiculite particles.

Figure 4. Parameters mapping for the laboratory-made model clay sample. Color-code mapping of (a) mineral content (N_i), (b) degree of preferred orientation ($\langle P_2 \rangle_i$), and (c) main angle deviation (Δ_i) of symmetry axis for i = vermiculite, mica, and kaolinite (maps of width=2.925 mm and length=7.8 mm). For (b) and (c), histograms on the top illustrates the number of particles N_i as a function of $\langle P_2 \rangle_i$ or Δ_i , respectively. These histograms correspond to individual sub-beds (top, middle, or bottom) defined using the image mask reported in Fig. S1.

655

656 **Figure 5.** BSE SEM map of the topsoil surface of the KCl plot from LTBF experiment of INRAE Versailles.

657 (a) Overall image with dashed white line separating the sedimentary from the structural crust. The
658 solid rectangle indicates the region of interest for synchrotron 2D- μ XRD analysis. (b) Region analysed
659 by synchrotron 2D- μ XRD-mapping method and showing the 4 deposition zones detected and
660 separated by dashed lines. The three rectangles are zoomed in (c), (d), and (e).

661

662 **Figure 6.** Averaged $I^{av.}(Q)$ pattern and definition of mineral boundaries for extraction of intensity

663 $I_i(\tau)$ associated to each mineral i for topsoil surface of the KCl plot from LTBF experiment of INRAE
664 Versailles. C= chlorite, I/M= illite/mica, K=kaolinite, Q=quartz, and F=Feldspars. The vertical grey bar
665 indicate a Y-scale multiplication by 8 of the low-angle region. The vertical dashed line corresponds to
666 the Q -boundary limit between the (001) reflection of kaolinite and the (002) reflection of chlorite.

667

668 **Figure 7.** Synchrotron 2D- μ XRD color-code mapping of the ROI (Fig. 5b) for the topsoil surface of the
669 KCl plot from LTBF experiment of INRAE Versailles. The four deposition zones (1-4) detected on
670 BSE SEM map are separated by dashed lines. Intensity mapping is shown in (a) for hk bands of clay
671 phases (I_{hk}) and in (b) for quartz (I_Q). In (c) the four clay microlayers (A-D) are surrounded by solid
672 lines and superimposed to I_{hk} map (a). (d) 2D map of the resin factor F according to Eq. (3).

673

674 **Figure 8.** Parameters mapping for the ROI (Fig. 5b) analysed by synchrotron 2D- μ XRD-mapping method
675 from the topsoil surface of the KCl plot from LTBF experiment of INRAE Versailles. Color-code mapping
676 of (a) mineral content (N_i), (b) degree of preferred orientation ($\langle P_2 \rangle_i$), and (c) main angle deviation
677 (Δ_i) of symmetry axis for i = illite/micas, chlorite, and kaolinite. The four deposition zones detected
678 on BSE SEM map of the ROI are separated by dashed lines. For (b), histograms on the bottom illustrate
679 the number of particles N_i as a function of $\langle P_2 \rangle_i$. These histograms correspond to the four clay
680 microlayers (A-B) defined in Fig. 7c using the mask reported in Fig. S3.

SUPPLEMENTARY DATA (S.D.)

Figure S1. Image mask allowing the definition of the deposition steps and extraction of clay parameters for specific sub-beds relative to vermiculite, mica, and kaolinite (see Fig. 4) for the laboratory-made model clay sample.

Table S1. Q -boundaries used to create parameter maps for the different phases in the topsoil surface of the KCl plot from LTBF experiment of INRAE Versailles.

Figure S2. Discrimination between kaolinite and chlorite (002) contribution for the topsoil surface of the KCl plot from LTBF experiment of INRAE Versailles. Separation between kaolinite (001) reflection and (002) reflection of chlorite is set at $Q=0.885 \text{ \AA}^{-1}$ (Table S1). Color-code mapping of (a) mineral content (N_i), (b) degree of preferred orientation ($\langle P_2 \rangle_i$), and (c) main angle deviation (Δ_i) of symmetry axis for $i =$ (001) reflection of chlorite, (002) reflection of chlorite, and kaolinite. The similar maps obtained for (001) or (002) reflections of chlorite, as well as the difference between the maps obtained for chlorite and kaolinite (lower values in N for clay microlayer A for chlorite, lower Δ value in clay microlayer A for kaolinite), validate the correct discrimination between the two minerals.

Figure S3. Image mask allowing the definition of the four clay microlayers (A-D) of the ROI for the topsoil surface of the KCl plot from LTBF experiment of INRAE Versailles (see Figs. 7 and 8).

Figure 1

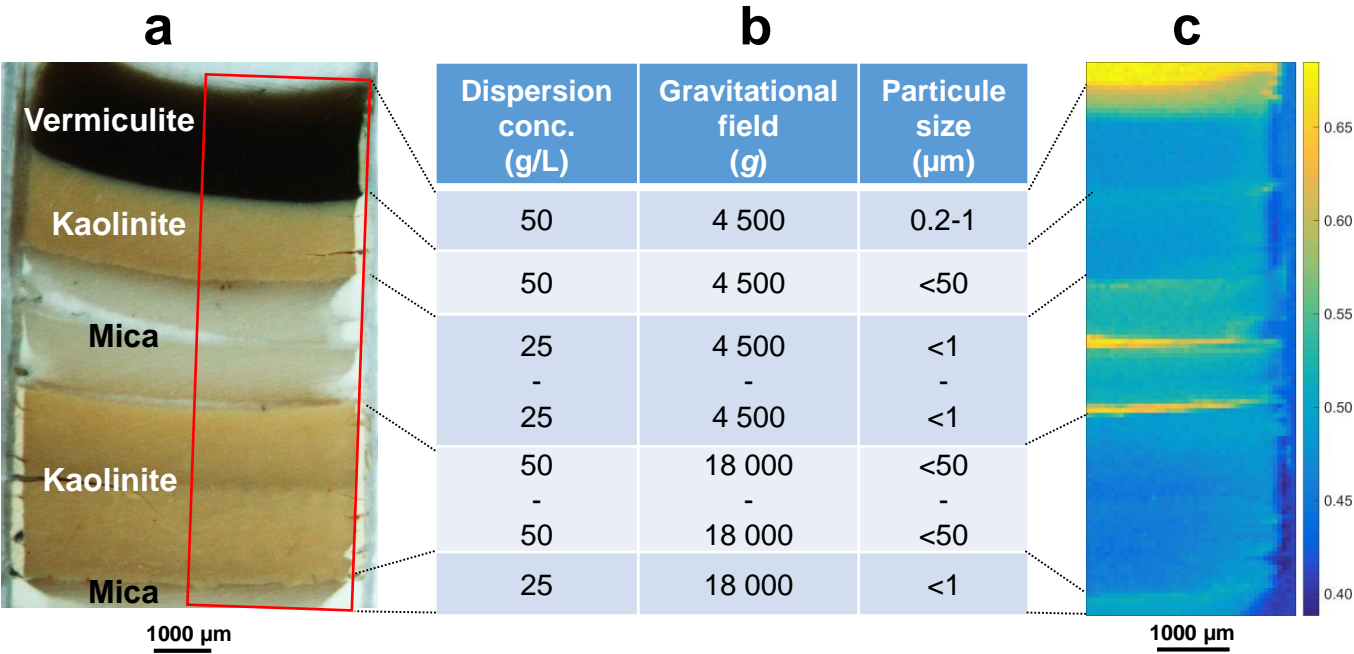


Figure 2

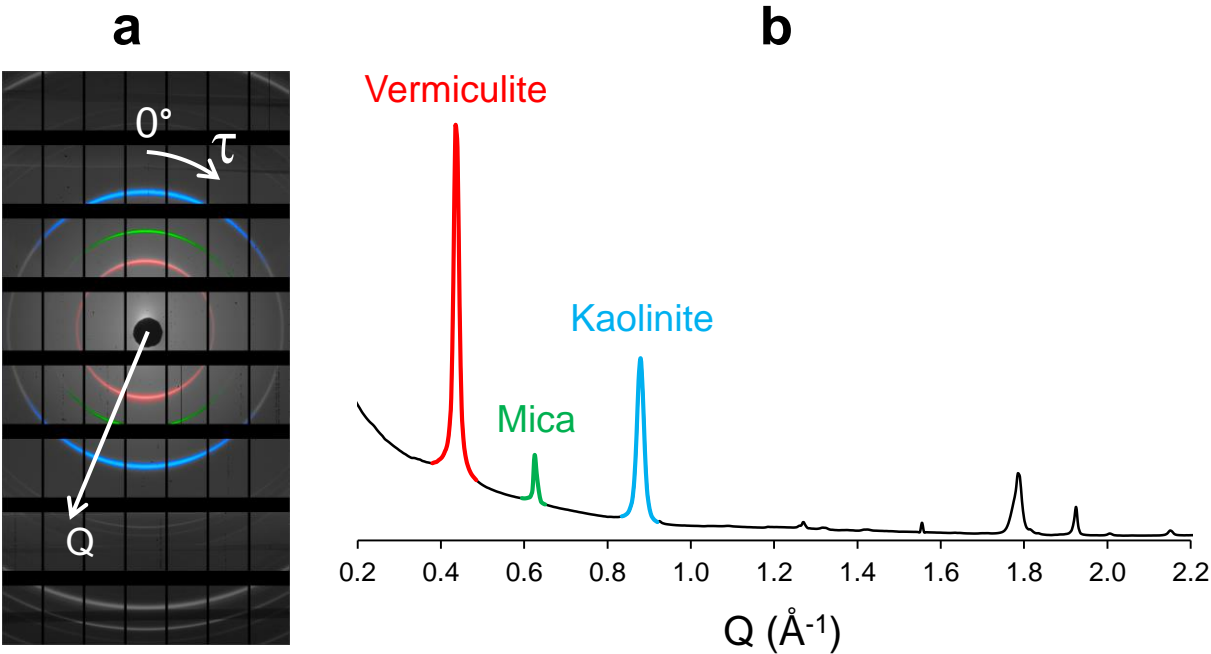


Figure 3

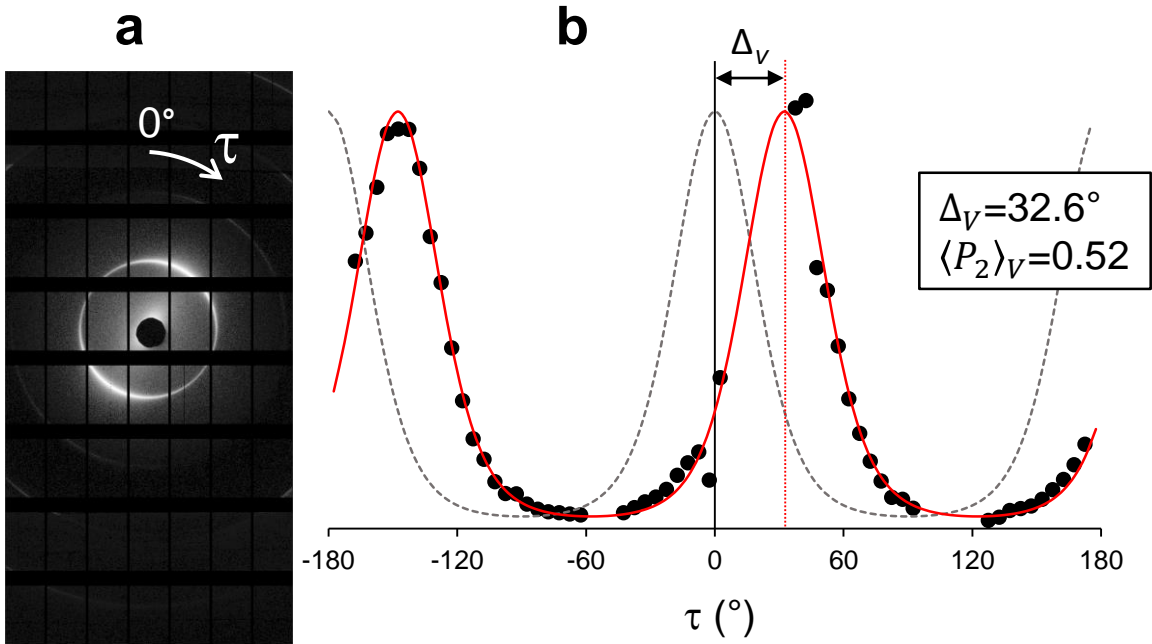


Figure 4

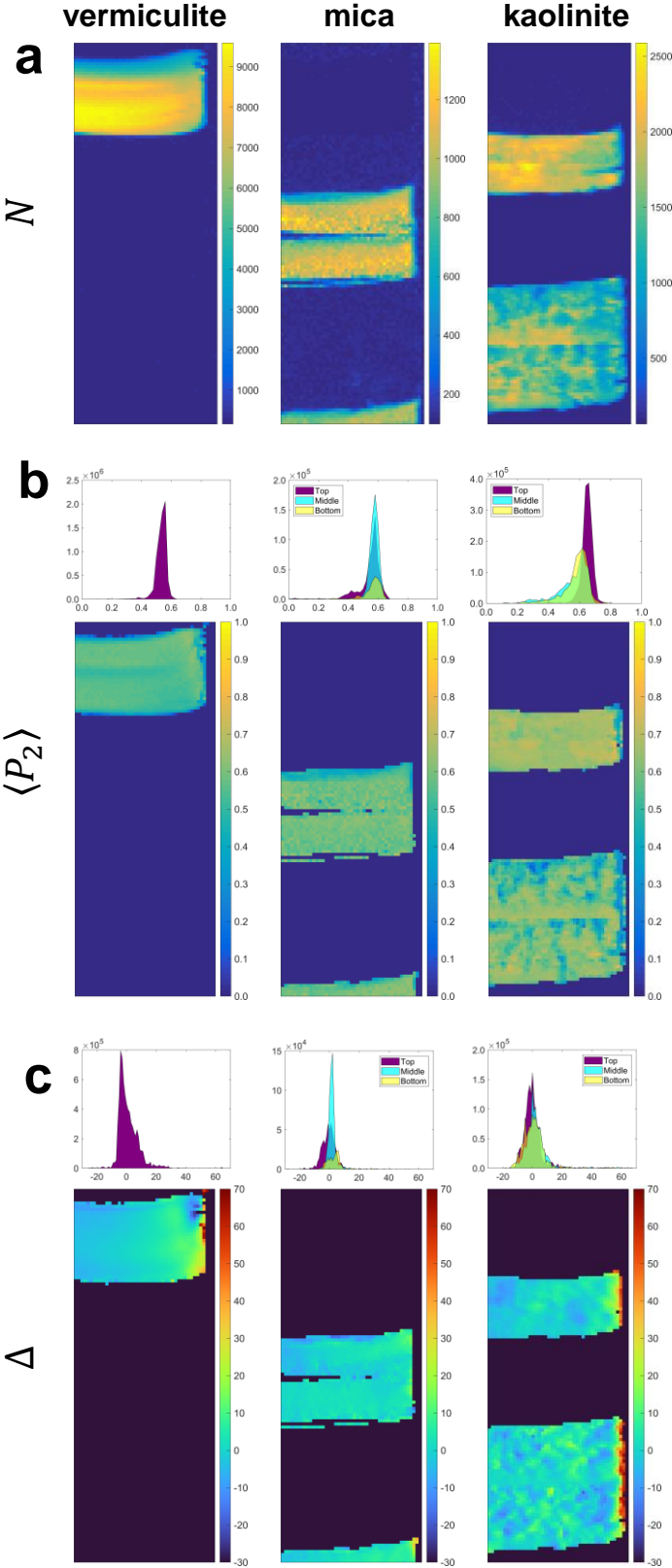


Figure 5

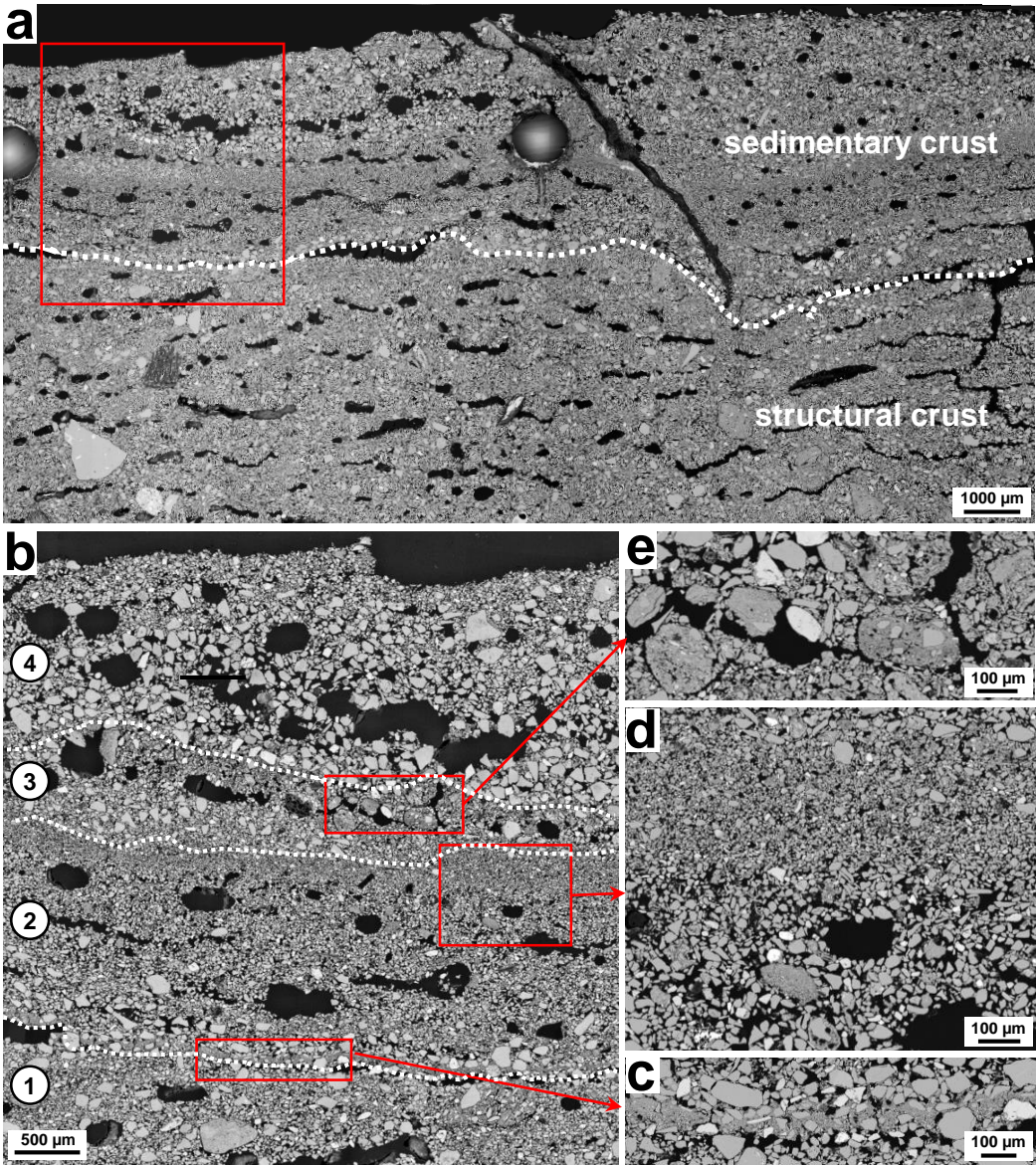


Figure 6

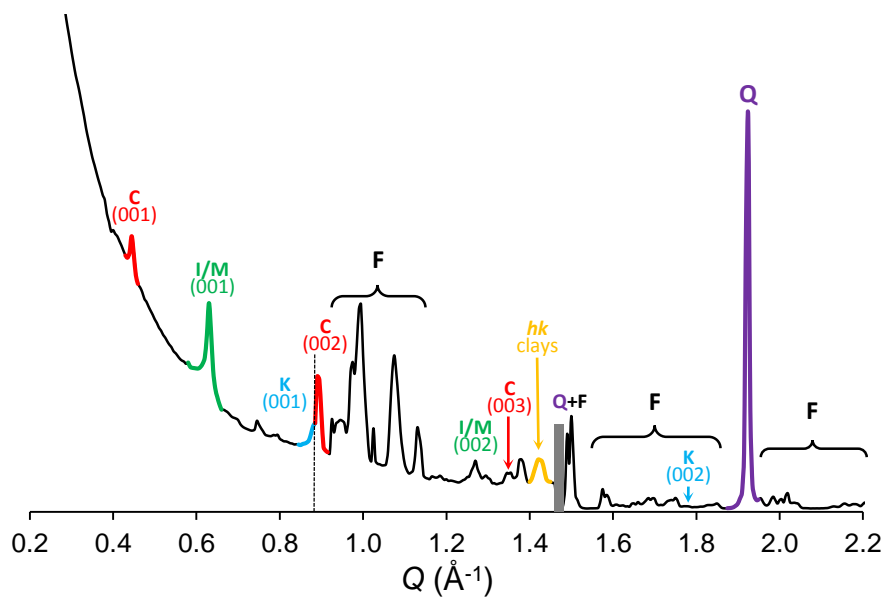


Figure 7

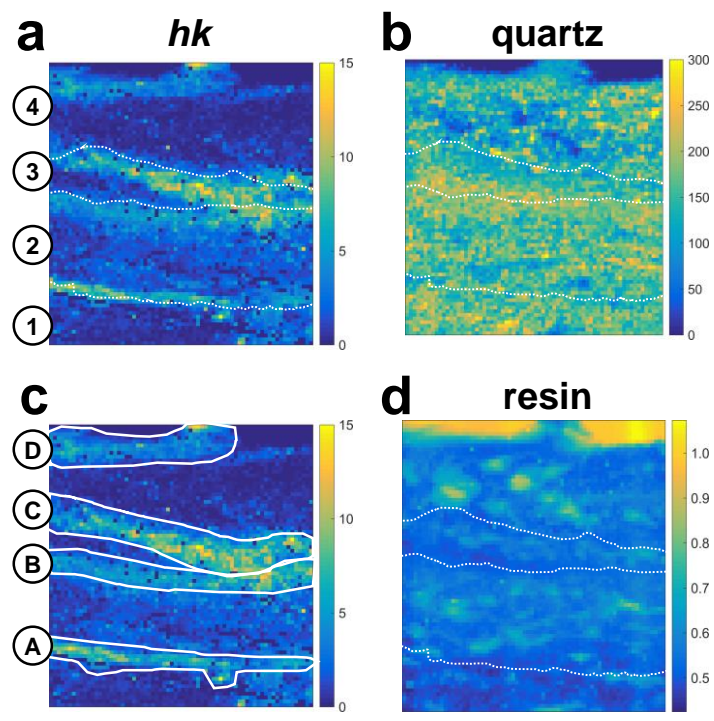


Figure 8

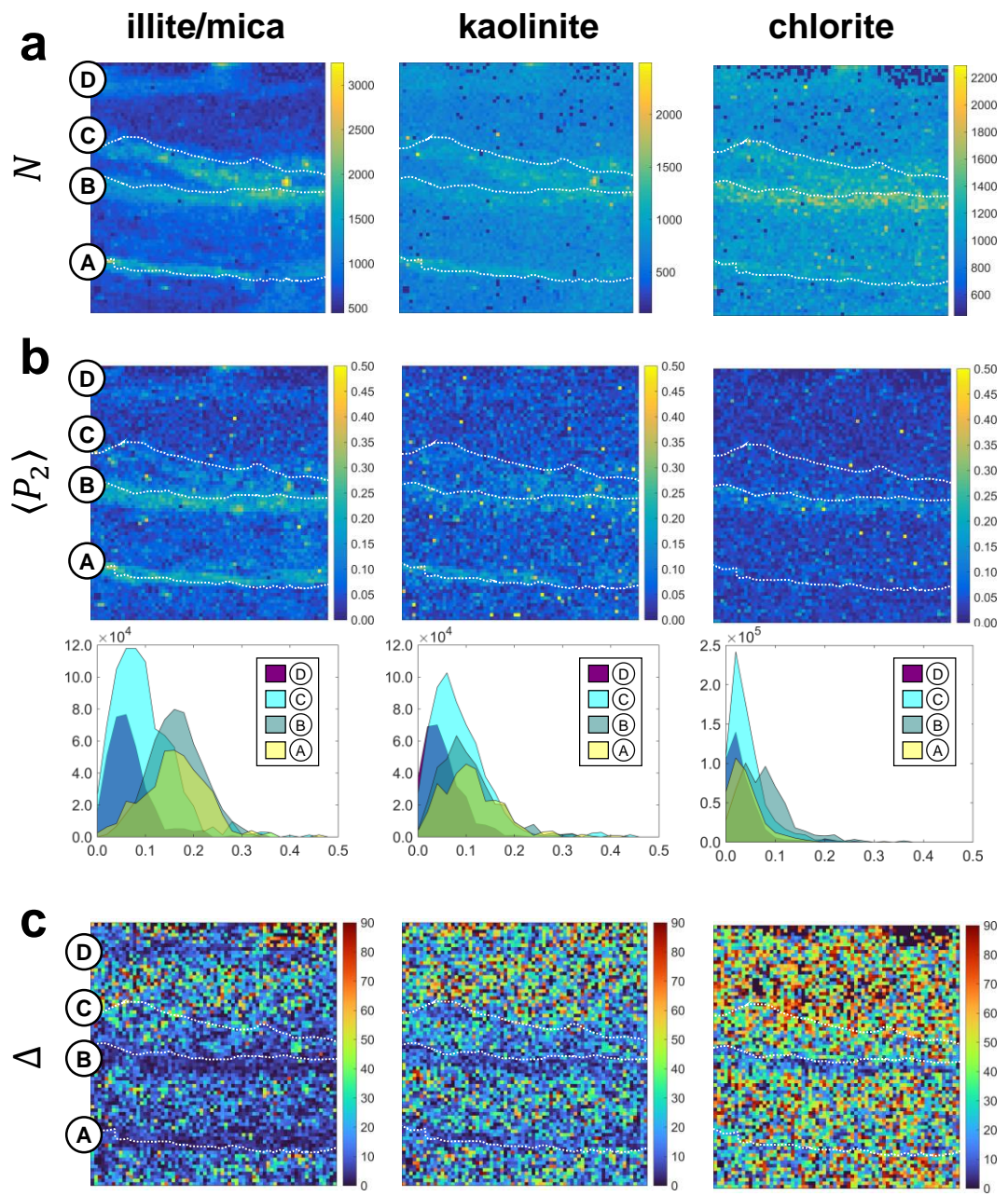


Figure S1

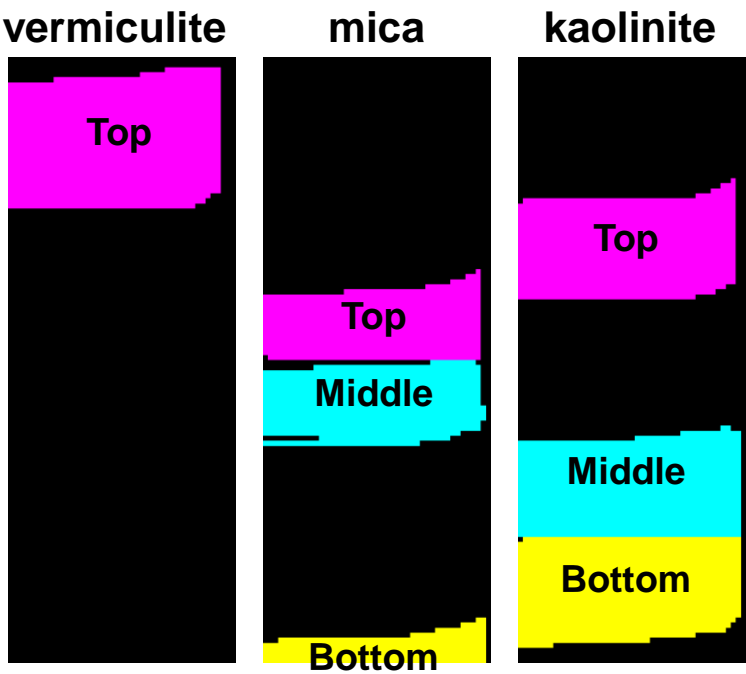


Figure S2

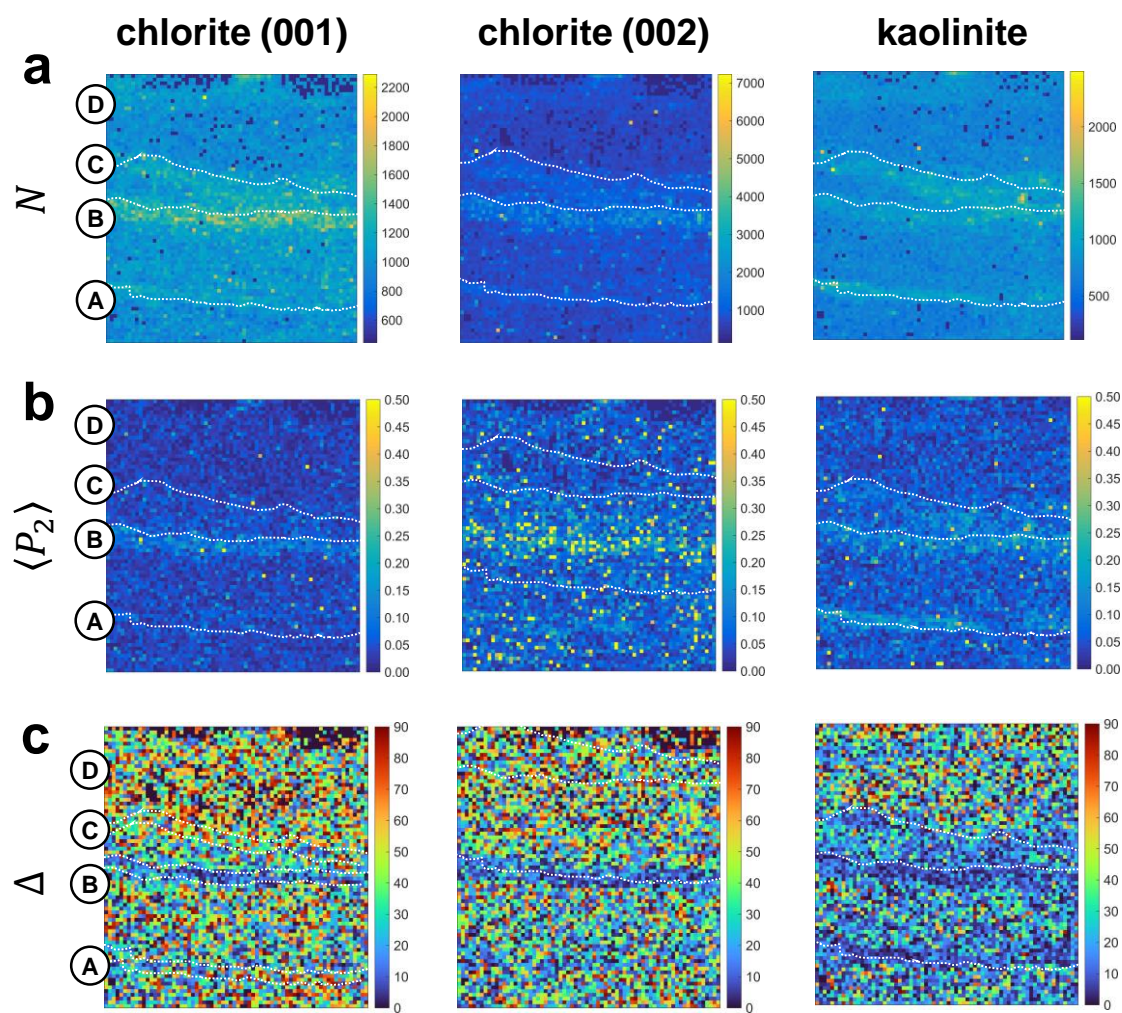


Figure S3

